Computational Materials Science 245 (2024) 113285

Contents lists available at ScienceDirect

Computational Materials Science

journal homepage: www.elsevier.com/locate/commatsci

Full Length Article

A comparative first-principles study on the physical properties of $Gd_2Zr_2O_7$ weberite and pyrochlore

Chenguang Liu [a,*], Rongrong Gao [a], Yue Xia [b], Xiaoyi Xia [a], Tan Shi [e], Qing Peng [f,g,h], Fei Gao [d,*], Yuhong Li [c,*]

[a] College of Nuclear Equipment & Nuclear Engineering, Yantai University, Yantai 264005, China
[b] School of Nuclear Science and Technology, University of South China, Hengyang 421001, China
[c] School of Nuclear Science & Technology, Lanzhou University, Lanzhou 730000, China
[d] Nuclear Engineering & Radiological Sciences, University of Michigan, Ann Arbor, MI 48109, USA
[e] School of Nuclear Science & Technology, Xi'an Jiaotong University, Xi'an 710049, China
[f] State Key Laboratory of Nonlinear Mechanics, Institute of Mechanics, Chinese Academy of Sciences, Beijing 100190, China
[g] Center of Materials Science and Optoelectronics Engineering, University of Chinese Academy of Sciences, Beijing 100049, China
[h] Guangdong Aerospace Research Academy, Guangzhou 511458, China

ARTICLE INFO

Keywords:
Weberite
Pyrochlore
First principles calculations
Physical properties

ABSTRACT

A comparative analysis of the physical properties of $Gd_2Zr_2O_7$ weberite and pyrochlore is conducted using first-principles methods. The structural characteristics of $Gd_2Zr_2O_7$ pyrochlore and weberite are examined at the atomic site, local coordination, and lattice parameter levels. The findings from ab initio molecular dynamics simulations and experimental data confirm the existence and stability of the $Gd_2Zr_2O_7$ weberite structure at 300 K. The formation of cation antisite defects is calculated to be more facile in the weberite lattice compared to pyrochlore. The formation energy of vacancy defects is strongly correlated to the distinct defect configurations. The calculations further highlight that $Gd_2Zr_2O_7$ weberite exhibits mechanical properties comparable to pyrochlore. The insulating nature, chemical bonding characteristics, and charge states of individual atoms in weberite and pyrochlore are elucidated through analysis of the partial density of states and Bader charges.

1. Introduction

Pyrochlore oxides have garnered significant public attention and research interest, owing to their diverse applications, including thermal barrier coatings [1,2], superconductors [3], inter matrices of nuclear fuel [4], solid electrolytes[5] and nuclear waste form [6–9]. The versatility of pyrochlores in these applications arises from their chemical and structural flexibility, as well as their interesting disordering process under extreme conditions [10–14]. For example, certain pyrochlores ($A_2B_2O_7$) exhibit phase transitions from ordered to disordered (O-D) or amorphous (O-A) phase under irradiation. A correlation exists between the propensity for phase transitions and the energy expenditure associated with cation disordering of pyrochlores [13,15]. The tendency of the pyrochlore amorphization intensifies with the escalating energy cost of cation disorder, characterized by the swapping of A and B cations within pyrochlore. Previous studies have elucidated the disordered structure, where A and B cations interchange positions and anion Frenkel pairs result in a random distribution of oxygen vacancies [13]. The disordered structure resembles that of the mineral fluorite, with the unit cell parameter of pyrochlore being halved [15]. However, recent experimental research utilizing neutron total scattering has revealed that local ordered domains contribute to the formation of large-scale disordered pyrochlore structures [16]. The local order structure is identified as an orthorhombic weberite model with space group *Ccmm* crystal symmetry [16]. The findings suggest that the O-D phase transition in pyrochlores is more intricate than previously understood.

Further researches have been conducted to investigate the mechanism underlying the formation of the local ordered domains and the interplay between the weberite structure and pyrochlore[17–19]. The local site disorder of zirconate pyrochlores was studied by Zhao *et al.* [17] based on oxygen migration and cation antisite using first principles calculations. According to their results, O_{48f} migrates to the closest intrinsic 8a vacancy, facilitating the local weberite configurations. Matsumoto *et al.* [20] systematically studied the crystal structures and

* Corresponding authors.
E-mail addresses: liuchg@ytu.edu.cn (C. Liu), gaofeium@umich.edu (F. Gao), liyuhong@lzu.edu.cn (Y. Li).

https://doi.org/10.1016/j.commatsci.2024.113285
Received 1 May 2024; Received in revised form 30 July 2024; Accepted 9 August 2024
Available online 15 August 2024

energetics of $A_2B_2O_7$ (A=Lu-La, B=Zr, Hf, Sn and Ti) compounds, revealing the stability of the weberite structure increases with a decrease in the radius of the A cation, relative to the pyrochlore structure. Kowalski *et al.* [21] argue that $Ln_2Hf_2O_7$ and $Ln_2Zr_2O_7$weberite is more stable for lanthanides after Dy and Gd than the corresponding pyrochlore structure from the perspective of formation enthalpy.

Pyrochlore undergoes a phase transition under high pressure, and similarly, the emergence of locally ordered weberite domains has been observed during this transition. The high-pressure structural modifications of rare earth hafnate pyrochlores have been systematically investigated by Turner *et al.* [22] in experiments. Their findings reveal that rare earth hafnate quenched from 50 GPa shows a local weberite-type structure from the Raman spectra. To date, no systematic research has been conducted on weberite and pyrochlore with identical chemical formulas; hence, this study aims to undertake a comparative analysis on the physical properties of $Gd_2Zr_2O_7$ weberite and pyrochlore using first principles method. The outcomes of this study could enhance our understanding of the distinctions and interrelations between weberite and pyrochlore, encompassing structural properties, defect formation energy, mechanical properties and electronic properties. This work could provide valuable insights into the disordering process in pyrochlore and promote the application of complex oxides in extreme environments.

2. Computational and experimental methods

The Vienna Ab-initio Simulation Package (VASP) has been used for all density functional theory calculations [23,24]. For the electron–ion interactions, the projector augmented wave (PAW) method [25] is used, whereas the exchange–correlation potentials are described by Perdew-Burke-Ernzerhof (PBE) [26] under generalized gradient approximation (GGA). The $Gd_2Zr_2O_7$ weberite structure with 44 atoms is constructed by using the special quasi-random structure (SQS) [27] method. For $Gd_2Zr_2O_7$ weberite, a 3 × 4 × 4 *k*-points grid and the plane wave cutoff energy of 600 eV are applied to the simulation. For $Gd_2Zr_2O_7$ pyrochlore, a primitive cell with 22 atoms is employed and a 4 × 4 × 4 *k*-points grid in reciprocal space and the plane wave cutoff energy of 600 eV are applied to the simulations. The electronic configurations for Gd, Zr and O are $5p^6 5d^1 6s^2$, $4s^2 4p^6 4d^2 5s^2$ and$2s^2 2p^4$, respectively. For *ab initio* molecular dynamics (AIMD) calculations, the 1 × 1 × 1 mesh with the original Γ point and the cutoff energy of 400 eV is used. An orthorhombic supercell structure with 132 atoms as shown in Fig. 1(a) and the NPT ensemble with three-axes periodic boundary conditions is carried out for the calculations. At 300 K, the supercell is equilibrated for 3000-time steps, and the total time is 9 ps.

Experimentally, a solid-state reaction is used to prepare polycrystalline $Gd_2Zr_2O_7$ samples. Gd_2O_3 (99.99 % purity), ZrO_2 (99.99 % purity) are selected as raw materials. Using a 13 mm diameter stainless steel die, ball milled powders are pressed into pellets at 450 MPa. After being sintered for 24 h at 1100 °C, the pellets are reground into powder, repressed into pellets, and then sintered for a further 48 h at 1100 °C. The sintered samples are characterized by XRD using a PANalytical X'Pert Pro X-ray diffractometer, with a scanning range of 10°–70° and step size of 0.02°.

3. Results and discussion

3.1. Structural properties of $Gd_2Zr_2O_7$ weberite

$Gd_2Zr_2O_7$ weberite, with space group *Ccmm*, has an orthorhombic structure and four formula units within a unit cell as shown in Fig. 2. Gd and Zr cations occupy 4*a*, 4*b* and 8 *g* sites. The 4*a* and 4*b* lattice sites with 8- and 6-fold coordination are fully occupied by half of the Gd and Zr cations. The 8 *g* lattice sites with 7-fold coordination are shared by the remaining half. The 16 *h* and three 4*c* lattice sites are occupied by the O anions and an intrinsic ordered vacancy is located at a fourth 4*c* site [16]. Zr cation coordinates with two intrinsic 8*a* vacancies and six 48*f* oxygen atoms and Gd cation coordinates with six 48*f* oxygen atoms and two 8*b* oxygen atoms in $Gd_2Zr_2O_7$ pyrochlore. Fig. 3 depicts the distinction and correlation between the $Gd_2Zr_2O_7$ weberite and the pyrochlore structure.

The optimized lattice constants and the bond lengths in $Gd_2Zr_2O_7$ weberite are presented in Table 1, along with the results of theoretical calculations. The lattice constants of orthorhombic unit cell are a = 10.47 Å, b = c = 7.42 Å, which are in agreement with Zhao's results [17]. The bond length of < Gd-O>ranges between 2.258 Å and 2.721 Å and the < Zr-O>ranges from 2.054 Å to 2.437 Å. Therefore, the lengths of the same type bond are different in a weberite unit cell which indicate that the multiple polyhedrons formed by Gd-O and Zr-O are irregular in shape.

The AIMD simulation results depicted in Fig. 1(b) reveal that the atomic positions in the final state of $Gd_2Zr_2O_7$ weberite exhibit minimal variation compared to the initial state, following 3000 steps of

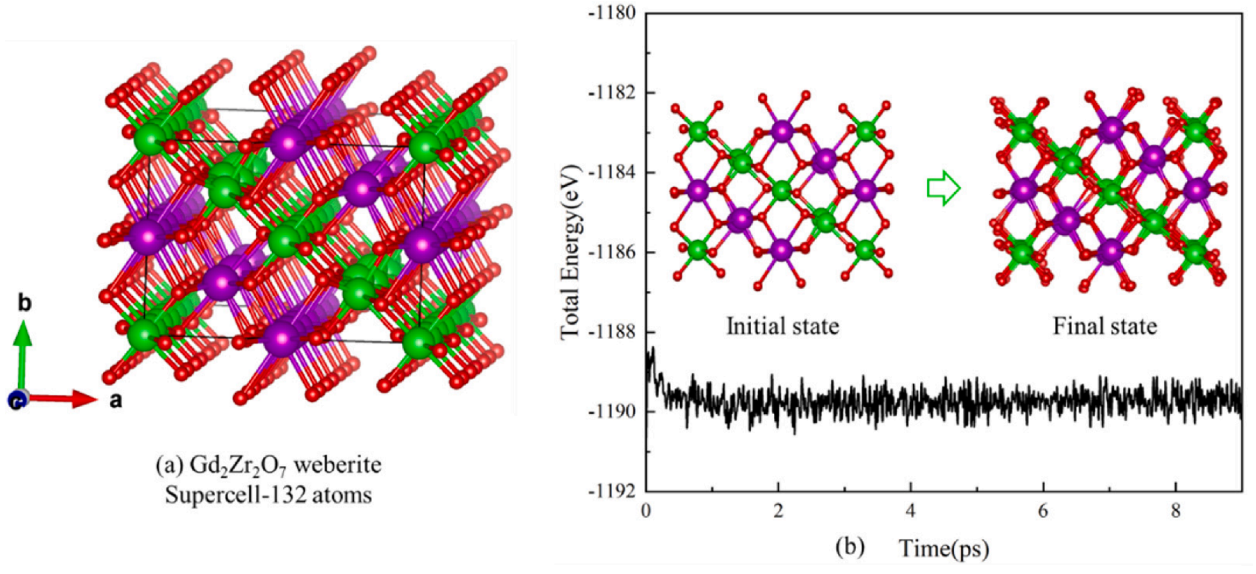

Fig. 1. (a) $Gd_2Zr_2O_7$ weberite supercell containing 132 atoms used for AIMD simulations. (b) Evolution of total energy of weberite with time from initial state to final state.

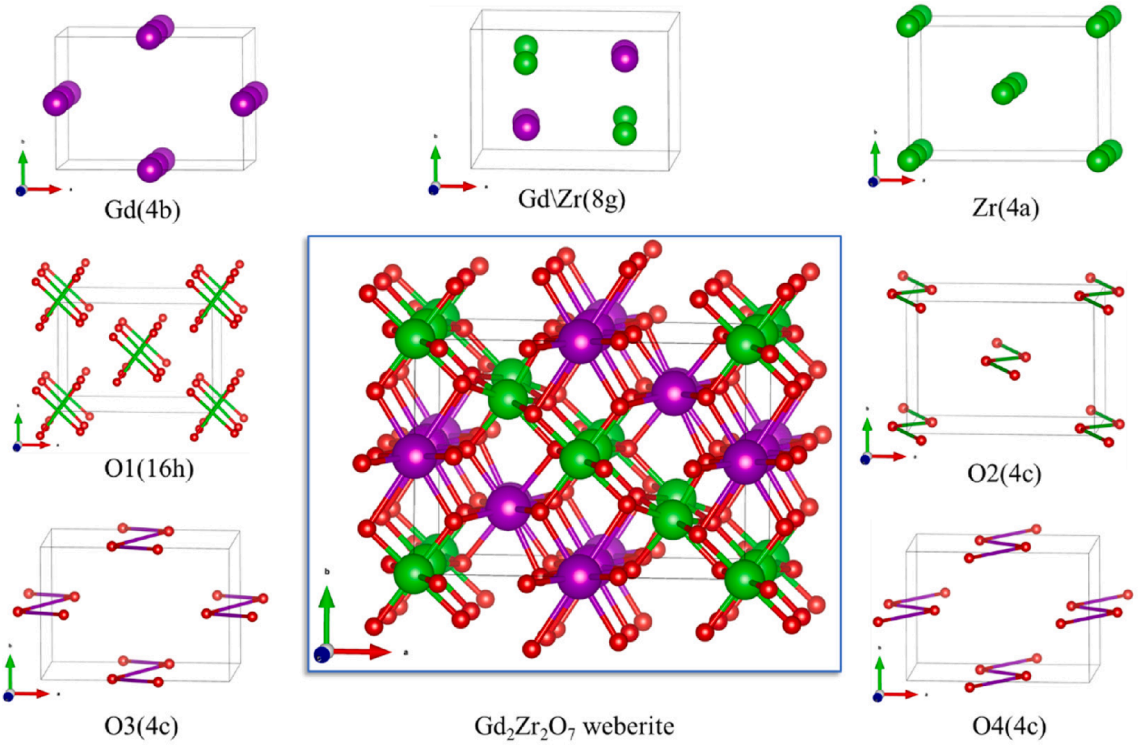

Fig. 2. The structure of $Gd_2Zr_2O_7$ weberite and Wyckoff position occupied by each atom. Gadolinium, zirconium, and oxygen atoms are represented by purple, green, and red spheres, respectively.

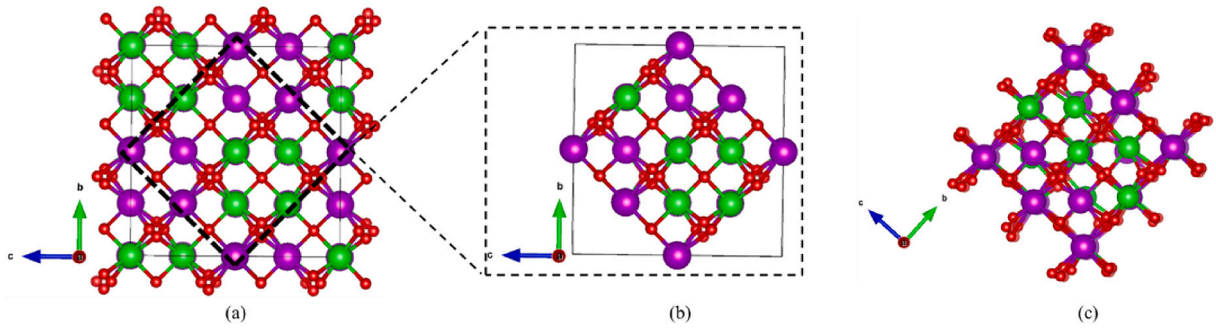

Fig. 3. The distinction and relation between the $Gd_2Zr_2O_7$ pyrochlore and weberite structure. (a) an 88-atom pyrochlore unit cell. (b) Local structure of pyrochlore in top view along *a* axis. (c) a 44-atom weberite unit cell. The relationship between pyrochlore and weberite in the unit cell lattice parameters is as follows: $a_P=a_W$ and $b_W=c_W=2^{-1/2}a_P$. (a_P is the lattice constant of pyrochlore, a_W, b_W, c_W is the lattice constant of weberite.).

Table 1
The calculated lattice constant (Å) and bond distances (Å) for $Gd_2Zr_2O_7$ weberite.

Lattice constant	a = 10.47 Å, b = c = 7.42 Å
Other calc [17].	a = 10.49 Å, b = c = 7.42 Å
$< Gd_{4d}\text{-}O_{4c} >$	2.346 Å ~ 2.367 Å
$<Gd_{4d}\text{-}O_{16h}>$	2.402 Å ~ 2.721 Å
$<Gd_{8g}\text{-}O_{16h}>$	2.299 Å ~ 2.377 Å
$<Gd_{8g}\text{-}O_{4c}>$	2.258 Å~2.403 Å
$<Zr_{4a}\text{-}O_{16h}>$	2.075 Å ~2.078 Å
$< Zr_{4a}\text{-}O_{4c} >$	2.089 Å
$<Zr_{8g}\text{-}O_{16h}>$	2.079 Å ~2.437 Å
$<Zr_{8g}\text{-}O_{4c}>$	2.054 Å~2.187 Å

relaxation at 300 K. Moreover, the total energy of $Gd_2Zr_2O_7$ weberite supercell fluctuates around −1189 eV, indicative of the stability of the structure at 300 K.

According to the experiments of the solid-phase method, when the sintering temperature reaches 1100 °C, two weberite-type diffraction peaks appear at around 20° in the XRD patterns of the $Gd_2Zr_2O_7$ samples (marked with asterisk in the Fig. 4), which indicates the existence of the weberite structure in $Gd_2Zr_2O_7$ compounds. To be noted, we did not obtain a single-phase weberite-type $Gd_2Zr_2O_7$ by solid-phase method, and the XRD of the $Gd_2Zr_2O_7$ at 1100℃ represents a coexistence of both pyrochlore and weberite structures. The asterisk marked diffraction peaks in Fig. 4 can be indexed as (111) and (201) in weberite-type $Gd_2Zr_2O_7$. The odd Miller indices (111) and (201) are the characteristic diffraction maxima in weberite-type $Gd_2Zr_2O_7$, whereas the even Miller indices such as (222), (400), (422) are correspond to the parent fluorite structure.

3.2. Cation antisite defect in $Gd_2Zr_2O_7$ weberite

For complex oxides, an important role is played by the cation disorder in the relative stability of the structure under extreme conditions. For example, the radiation tolerance of pyrochlores has a strong

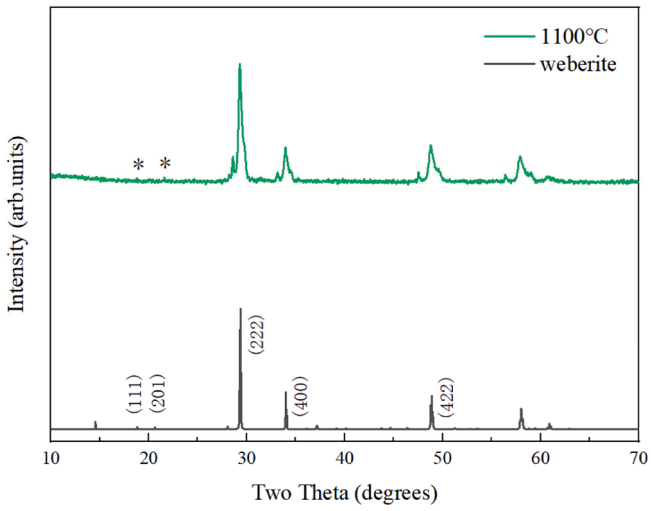

Fig. 4. XRD patterns of $Gd_2Zr_2O_7$ compounds at 1100℃ are compared with the XRD pattern of $Gd_2Zr_2O_7$ weberite obtained from the structure in our first principles calculations.

connection with the ability of the cation disorder [12]. Pyrochlore and weberite both form fluorite structures with ordered cations and vacancies, but have different unit cell sizes and symmetry. [16,17]. Furthermore, the weberite structure can be seen as one of the ordered structures of pyrochlore-related structures [28]. As such, it is essential to further investigate the role of cation antisite defect in $Gd_2Zr_2O_7$ weberite due to the close relationship between weberite and pyrochlore.

Different configurations of cation antisite defects in the cation sublattices are considered and shown in Fig. 5. The formation energy of a cation antisite defect is generally calculated to assess the ease of forming the cation antisite defect using the following equation [29,30]:

$$E_f^{CA} = E_{tot}^{CA} - E_{tot}$$

Where E_{tot}^{CA} is the total energy of a relaxed $Gd_2Zr_2O_7$ weberite cell with a cation antisite defect pair and E_{tot} represents the total energy of the relaxed $Gd_2Zr_2O_7$ weberite cell. The calculated results are shown in Fig. 6, which reveal that exchange of Gd(8 g) and Zr(8 g) cations produces the most readily formed cation antisite defects, followed by the configurations of Gd(4b)-Zr(8 g) and Gd(8 g)-Zr(4a), and the Gd (4b)-Zr(4a) is the least prone to form. In the (1 0 0) plane, it is noteworthy that the smallest formation energy occurs when Gd(8 g) and Zr (8 g) cations are exchanged. More importantly, the maximum value of cation antisite defect formation energy in $Gd_2Zr_2O_7$ weberite is 1.78 eV, which is still smaller than 2.08 eV in $Gd_2Zr_2O_7$ pyrochlore [30]. These results suggest that the cation antisite defect can be formed more easily in webertie lattice than that in pyrochlore. That is, the disordering process in cation sublattice in $Gd_2Zr_2O_7$ weberite may occur more easily than that in $Gd_2Zr_2O_7$ pyrochlore, which may be used to reflect the radiation damage resistance of them to some extent.

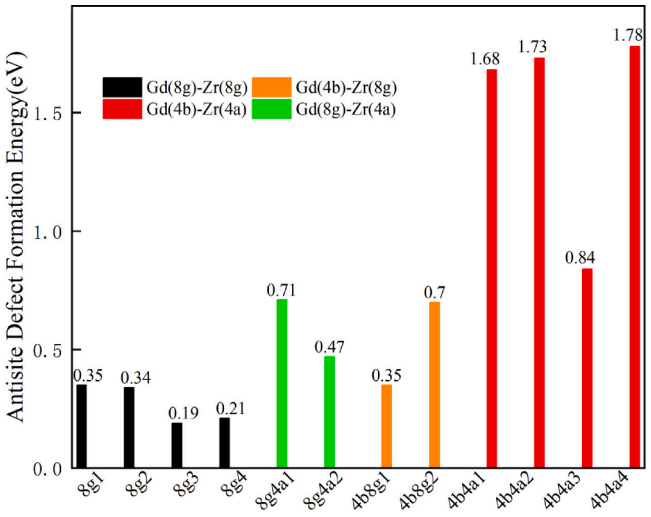

Fig. 6. The cation antisite defect formation energy of different configurations. The cation antisite defects: Gd(8 g)-Zr(8 g), Gd(4b)-Zr(8 g), Gd(4b)-Zr(4a) and Gd(8 g)-Zr(4a) are shown in black, orange, red and green block, respectively.

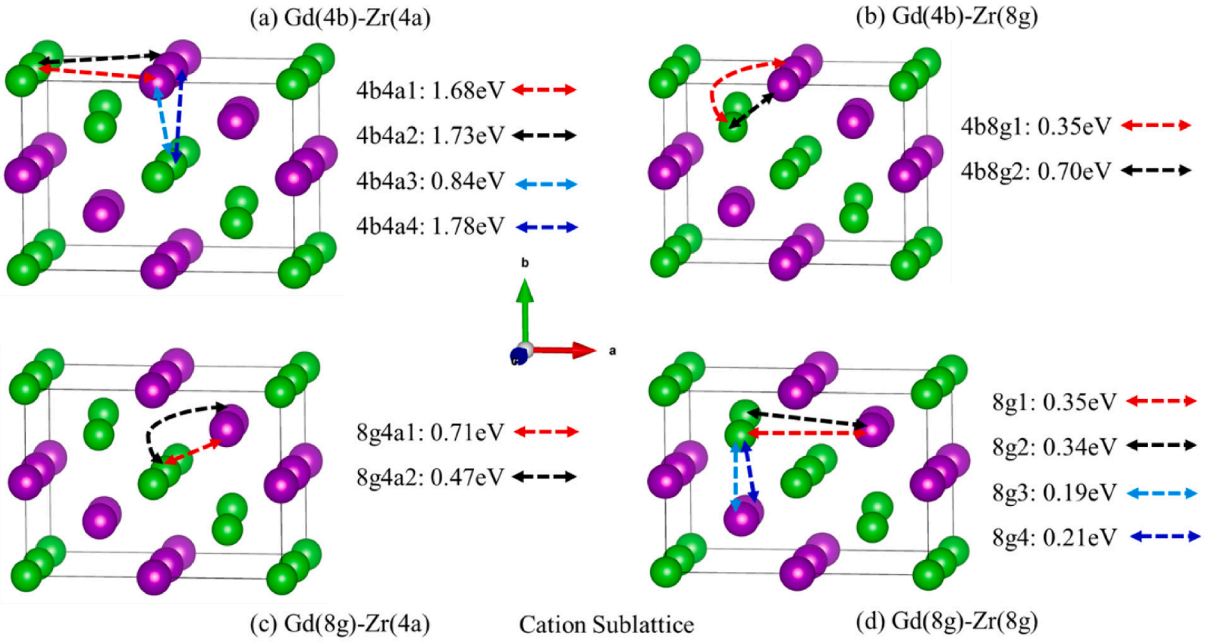

Fig. 5. The configuration of cation antisite defects in the cation sublattices. The cation antisite defect by exchanging the (a) Gd(4b)-Zr(4a), (b) Gd(4b)-Zr(8 g), (c) Gd (8 g)-Zr(4a) and (d) Gd(8 g)-Zr(8 g) cation along the directions indicated by arrows.

3.3. Vacancy defects in $Gd_2Zr_2O_7$ weberite and pyrochlore

The vacancy defect is one of the most important point defects to predict and understand the thermodynamic stability of materials under extreme conditions [31]. In this section, we estimate the formation tendency of formation of specific vacancy defects in $Gd_2Z_2O_7$ weberite and pyrochlore from the energetic point of view. The formation energy of a vacancy defect, E_f^v, are calculated using the following equation [31]:

$$E_f^v = E_w^v - E_w + \mu$$

where E_w^v is the total energy of $Gd_2Zr_2O_7$ weberite or pyrochlore containing a vacancy defect, E_w is the total energy of the relaxed $Gd_2Zr_2O_7$ weberite or pyrochlore structure, μ is the chemical potential of the corresponding atom. The chemical potential of Gd is obtained under the Gd_2O_3-rich and O_2-rich condition, $\mu_{Gd} = \frac{1}{2}(\mu_{Gd_2O_3} - 3\mu_O), \mu_O = \frac{1}{2}\mu_{O_2}$. The chemical potential of Zr is obtained under the ZrO_2-rich and O_2-rich condition, $\mu_{Zr} = \mu_{ZrO_2} - 2\mu_O, \mu_O = \frac{1}{2}\mu_{O_2}$. The total energies of optimized Gd_2O_3, ZrO_2 bulk and an O_2 molecule are used to determine the corresponding chemical potentials. The calculated vacancy defect formation energies are shown in Fig. 7.

For $Gd_2Zr_2O_7$ weberite, the vacancy formation energies of Gd(4*b*), Gd(8 *g*), Zr(4*a*), Zr(8 *g*), O1(16 *h*), O2(4*c*), O3(4*c*) and O4(4*c*) are 4.65, 3.99, 4.96, 5.45, 5.93, 6.34, 7.29 and 6.74 eV, respectively. The Gd vacancies at 8 *g* site and Zr vacancy at 4*a* site are easier to form based on the formation energy of cation vacancies. The formation energy of O vacancies at 16 h sites is lowest for anion vacancies. For $Gd_2Zr_2O_7$ pyrochlore, the vacancy formation energies of Gd(16*c*), Zr(16*d*), O1 (48*f*) and O2(8*b*) are 4.22, 5.04, 4.76 and 6.18 eV, respectively. The Gd vacancies are easier to form than Zr vacancies, and the O vacancies at 48*f* sites are easier to form than the O vacancies at 8*b* sites in $Gd_2Zr_2O_7$ pyrochlore. Contrasting to pyrochlore cases, the value of $V_{Gd(16c)}$ in pyrochlore is larger than $V_{Gd(4b)}$, but smaller than $V_{Gd(8g)}$ in weberite, and the value of $V_{Zr(16d)}$ in pyrochlore is comparable to that of the $V_{Zr(4a)}$ in weberite. The O vacancies at 48*f* sites in pyrochlore are most readily formed, followed by the O vacancies at 16 *h* sites in weberite.

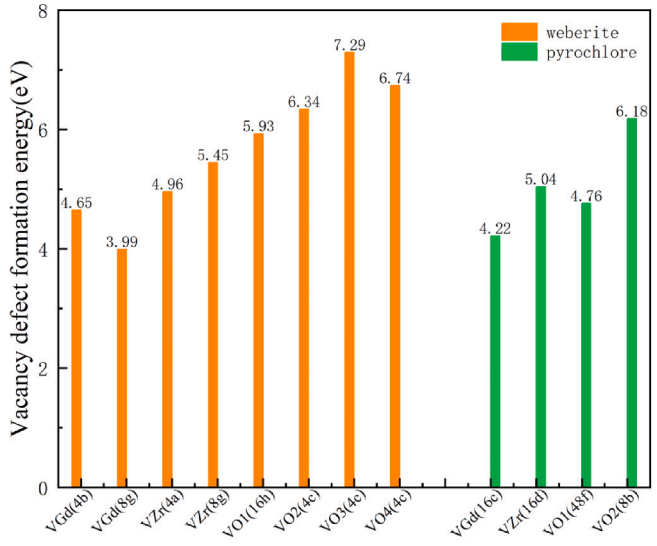

Fig. 7. The calculated vacancy defect formation energies of different defect configurations in $Gd_2Zr_2O_7$ weberite and pyrochlore. The vacancy defects in weberite and pyrochlore are color-coded orange and green, respectively.

3.4. Mechanical properties of $Gd_2Zr_2O_7$ weberite

The mechanical properties are further studied based on the optimized $Gd_2Zr_2O_7$ weberite structures. Orthorhombic phase has nine independent elastic constants: C_{11}, C_{22}, C_{33}, C_{44}, C_{55}, C_{66}, C_{12}, C_{13} and C_{23}. The calculated results for $Gd_2Zr_2O_7$ weberite are shown in Table 2. Based on the Voigt-Reuss-Hill approximation, the Voigt bulk modulus B_V, the Reuss bulk modulus B_R, the Voigt shear modulus G_V, the Reuss shear modulus G_R for an orthorhombic phase can be represented by the following formulae:

$$B_V = \left(\frac{1}{9}\right)[C_{11} + C_{22} + C_{33} + 2(C_{12} + C_{13} + C_{23})]$$

$$G_V = \left(\frac{1}{15}\right)[C_{11} + C_{22} + C_{33} + 3(C_{44} + C_{55} + C_{66}) - (C_{12} + C_{13} + C_{23})]$$

$$B_R = \Delta[C_{11}(C_{22} + C_{33} - 2C_{23}) + C_{22}(C_{33} - 2C_{13}) - 2C_{33}C_{12} + C_{12}(2C_{23} - C_{12}) + C_{13}(2C_{12} - C_{13}) + C_{23}(2C_{13} - C_{23})]^{-1}$$

$$G_R = 15\{4[C_{11}(C_{22} + C_{33} + C_{23}) + C_{22}(C_{33} + C_{13}) + C_{33}C_{12} - C_{12}(C_{23} + C_{12}) - C_{13}(C_{12} + C_{13}) - C_{23}(C_{13} + C_{23})]/\Delta + 3[(1/C_{44}) + (1/C_{55}) + (1/C_{66})]\}^{-1}$$

$$\Delta = C_{13}(C_{12}C_{23} - C_{13}C_{22}) + C_{23}(C_{12}C_{13} - C_{23}C_{11}) + C_{33}(C_{11}C_{22} - C_{12}^2)$$

Mechanical stability is determined by the following criteria:

$$C_{11} > 0,\ C_{22} > 0,\ C_{33} > 0,\ C_{44} > 0,\ C_{55} > 0,\ C_{66} > 0.$$

$$(C_{11} + C_{33} - 2C_{13}) > 0, (C_{22} + C_{33} - 2C_{23}) > 0.$$

$$[C_{11} + C_{22} + C_{33} + 2(C_{12} + C_{13} + C_{23})] > 0$$

$$(C_{11} + C_{22} - 2C_{12}) > 0$$

According to the Hill approximation, bulk modulus B and shear modulus G are given by: $B = \frac{1}{2}(B^V + B^R)$ and $G = \frac{1}{2}(G^V + G^R)$. The Poisson's ratio σ is given by: $\sigma = \frac{3B-2G}{6B+2G}$ and the Young's modulus E is given by: $E = \frac{9BG}{3B+G}$. A summary of all calculated results is shown in Table 2.

A Pugh index (A^P) is calculated to determine the malleability of $Gd_2Zr_2O_7$ weberite by: A^P=B/G, which measures the ductility of a material with a critical value of 1.75. [32]. The calculated Pugh index as shown in Table 2 is larger than 1.75, which indicates that $Gd_2Zr_2O_7$ weberite possesses a certain ductility. The Poisson's ratio σ is also calculated to assess the malleability of materials. The materials will exhibit ductile properties when σ is larger than 0.25. The result of σ for $Gd_2Zr_2O_7$ weberite is 0.28 (see Table 2), which confirms the conclusion drawn from the Pugh's index. In addition to these studies of weberite, we also compare the current findings with our previous computational data for $Gd_2Zr_2O_7$ pyrochlore in Ref.[30]. The bulk modulus, shear modulus and Young's modulus for weberite are slightly smaller than those of pyrochlore, but the Poisson's ratio and Pugh index of weberite are comparable to those of pyrochlore. From these observations, it thus can be concluded that $Gd_2Zr_2O_7$ weberite shows similar mechanical properties to those of pyrochlore.

Table 2
Elastic constants (C, GPa), shear modulus (G,GPa), bulk modulus (B, GPa), Young's modulus (E, GPa), Poisson's ratio (σ), and Pugh index (A^P) for $Gd_2Zr_2O_7$ weberite and pyrochlore.

$Gd_2Zr_2O_7$	C_{11}	C_{22}	C_{33}	C_{44}	C_{55}	C_{66}	C_{12}	C_{13}	C_{23}
Weberite	292.63	274.61	267.73	93.64	87.92	58.89	96.31	111.71	108.93
	B_V	B_R	B_H	G_V	G_R	G_H	E	σ	A^P
	163.21	140.38	151.79	82.62	74.83	78.73	201.37	0.28	1.93
pyrochlore	**C_{11}**	**C_{12}**	**C_{44}**	**B**	**G**	**E**	**σ**	**A^P**	
Ref. [30]	301.38	118.75	86.4	179.63	88.33	227.68	0.29	2.03	

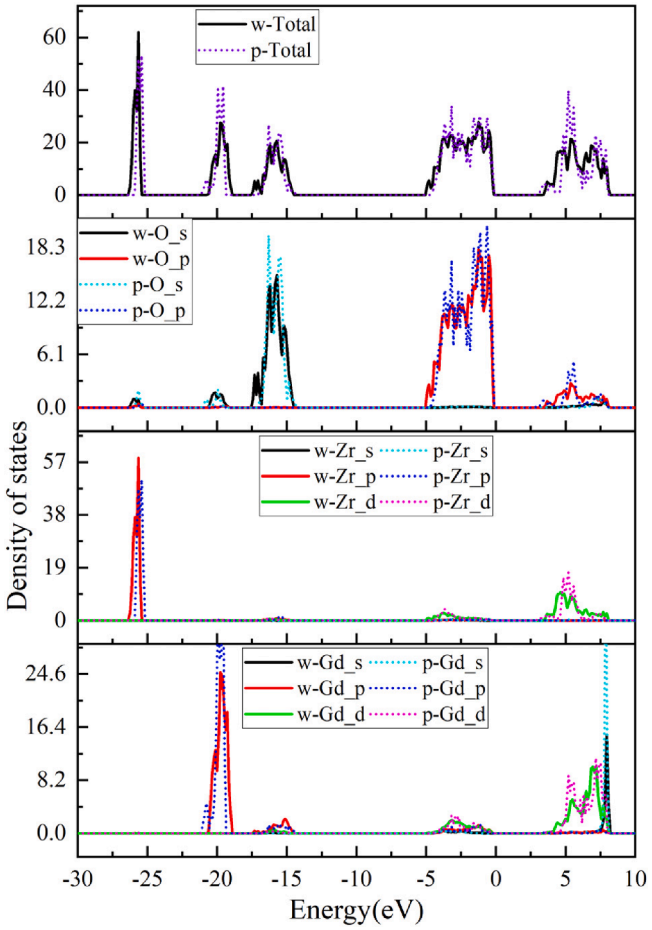

Fig. 8. Comparison of the projected density of states (PDOS) for $Gd_2Zr_2O_7$ weberite (w) and pyrochlore (p).

3.5. *Electronic properties of $Gd_2Zr_2O_7$ weberite and pyrochlore*

As shown in Fig. 8, partial densities of states (PDOS) are calculated to further study the electronic properties of $Gd_2Zr_2O_7$ weberite and pyrochlore. It can be found that the energy band gap for $Gd_2Zr_2O_7$ pyrochlore is 2.79 eV, which is slightly larger than 2.72 eV derived from the calculation by Zhao *et al.* [33]. However, as for $Gd_2Zr_2O_7$ weberite, the band gap is 3.56 eV. Both of them exhibit an insulating character. In the PDOS, the hybridization of O 2*p* with Gd 5*d*, Zr 4*d*, and a few Gd 5*p* states contributes to the valence band maximum (VBM); the hybridization of O 2*p* with Zr 4*d* and Gd 5*d* states contributes to the conduction band minimum (CBM). Comparing the PDOS of $Gd_2Zr_2O_7$ weberite and pyrochlore in Fig. 6, it is clear that the hybridization between O *p* states with Zr and Gd *d* states in weberite is slightly stronger than that in pyrochlore, suggesting that the stronger chemical bonds are formed in $Gd_2Zr_2O_7$ weberite.

A Bader charge is calculated in $Gd_2Zr_2O_7$ weberite and pyrochlore in order to obtain deeper insights into their charge states. Table 3 summarizes the results obtained. For weberite, the Bader charge of the same element is different at different sites. For example, the Bader charge of Gd at 4*b* site is 2.097 |*e*|, whereas the Bader charge is 2.051 |*e*| at 8 *g* site. The Bader charge of O at 16 *h* site is −1.316 |***e***|, but at three 4*c* sites the Bader charges are −1.318, −1.346 and −1.308 |*e*|, respectively. The average Bader charges of Gd and Zr in weberite are 2.074 |*e*| and 2.547 |*e*|, which is in accord with the Bader charges of Gd (2.075 |*e*|) and Zr (2.548 |*e*|) in pyrochlore. While the average Bader charge of O in weberite and pyrochlore is different, these are −1.322 |*e*| and −1.299 |*e*|, respectively. It indicates that the local electron transfer is related to the atomic lattice sites.

Table 3
Bader charge (|***e***|) for each atom in $Gd_2Zr_2O_7$ weberite and pyrochlore.

Pyrochlore		Weberite			
Element	Bader Charge (|*e*|)	Element	Bader Charge (|*e*|)	Element	Bader Charge (|*e*|)
Gd	2.075	**Gd(4b)**	2.097	**O(16 h)**	−1.316
Zr	2.548	**Gd(8 g)**	2.051	**O(4c1)**	−1.318
O(48*f*)	−1.327	**Zr(4a)**	2.531	**O(4c2)**	−1.346
O(8b)	−1.271	**Zr(8 g)**	2.563	**O(4c3)**	−1.308

4. Conclusions

We have compared the physical properties of $Gd_2Zr_2O_7$ weberite and pyrochlore employing first-principles methods. We provide a schematic representation to elucidate the differences and relationships between the structural properties of $Gd_2Zr_2O_7$ weberite and pyrochlore. The AIMD simulations and experimental findings collectively demonstrate that the $Gd_2Zr_2O_7$ weberite structure is indeed stable at 300 K. A comparative analysis of cation antisite and vacancy defect formation energies between weberite and pyrochlore indicates that cation antisite defects are more readily formed in the weberite lattice compared to pyrochlore, and the formation of vacancy defects is influenced by the availability of vacant lattice sites for the respective atoms. Our calculations reveal that both weberite and pyrochlore exhibit mechanical stability and share comparable mechanical properties. The analysis of electronic properties reveals that both structures exhibit insulating behavior, with the hybridization between O *p* states and Zr/Gd *d* states in weberite being marginally stronger than in pyrochlore, implying the formation of more robust chemical bonds in $Gd_2Zr_2O_7$ weberite.

CRediT authorship contribution statement

Chenguang Liu: Writing – review & editing, Supervision, Investigation, Funding acquisition, Formal analysis, Conceptualization. **Rongrong Gao:** Formal analysis. **Yue Xia:** Investigation, Formal analysis. **Xiaoyi Xia:** Investigation, Formal analysis. **Tan Shi:** Investigation, Formal analysis, Review & editing. **Qing Peng:** Investigation, Formal analysis, Funding acquisition, Review & editing. **Fei Gao:** Supervision, Review & editing. **Yuhong Li:** Supervision, Review & editing.

Declaration of competing interest

The authors declare that they have no known competing financial interests or personal relationships that could have appeared to influence the work reported in this paper.

Data availability

Data will be made available on request.

Acknowledgements

This work is supported by the National Natural Science Foundation of China (Grant No. 12205248, 12175093,11875046), the start-up fund from Yantai University to C.L. (Grant No. HD20B02.), Shandong Provincial Natural Science Foundation (Grant No. ZR2021QA028, ZR2023MA045) and Development Plan of Shandong Province Young Innovation Team of Higher Education Institutions (Grant No.2023KJ242). Q. P. would like to acknowledge the support provided by National Natural Science Foundation of China (Grant No. 12272378), High-level Innovation Research Institute Program of Guangdong Province (Grant No. 2020B0909010003), and LiYing Program of the Institute of Mechanics, Chinese Academy of Sciences (Grant No. E1Z1011001).

References

[1] L. Yang, C. Zhu, Y. Sheng, H. Nian, Q. Li, P. Song, W. Lu, J. Yang, B. Liu, Investigation of mechanical and thermal properties of rare earth pyrochlore oxides by first-principles calculations, J. Am. Ceram. Soc. 102 (2019) 2830–2840.
[2] F. Li, L. Zhou, J.-X. Liu, Y. Liang, G.-J. Zhang, High-entropy pyrochlores with low thermal conductivity for thermal barrier coating materials, J. Adv. Ceram. 8 (2019) 576–582.
[3] M. Hanawa, J. Yamaura, Y. Muraoka, F. Sakai, Z. Hiroi, Structural phase transition in the superconducting pyrochlore oxide $Cd_2Re_2O_7$, J. Phys. Chem. Solid 63 (2002) 1027–1030.
[4] G. Sattonnay, N. Sellami, L. Thomé, C. Legros, C. Grygiel, I. Monnet, J. Jagielski, I. Jozwik-Biala, P. Simon, Structural stability of $Nd_2Zr_2O_7$ pyrochlore ion-irradiated in a broad energy range, Acta Mater. 61 (2013) 6492–6505.
[5] A. Shlyakhtina, L. Shcherbakova, New solid electrolytes of the pyrochlore family, Russ. J. Electrochem. 48 (2012) 1–25.
[6] A.E. Ringwood, S.E. Kesson, N.G. Ware, W. Hibberson, A. Major, Immobilisation of high level nuclear reactor wastes in SYNROC, Nature 278 (1979) 219–223.
[7] R.C. Ewing, W.J. Weber, J. Lian, Nuclear waste disposal—Pyrochlore ($A_2B_2O_7$): Nuclear waste form for the immobilization of plutonium and "minor" actinides, J. Appl. Phys. 95 (2004) 5949–5971.
[8] N. Gumber, M. Shafeeq, S.K. Gupta, R. Phatak, U.K. Goutam, R. Kumar, R.V. Pai, Synthesis and feasibility studies of doping U at Ti site of $Y_2Ti_2O_7$ as a radioactive waste immobilization matrix, Dalton Trans. 52 (2023) 14170–14181.
[9] Y. Li, B. Uberuaga, C. Jiang, S. Choudhury, J. Valdez, M. Patel, J. Won, Y.-Q. Wang, M. Tang, D. Safarik, Role of antisite disorder on preamorphization swelling in titanate pyrochlores, Phys. Rev. Lett. 108 (2012) 195504.
[10] D. Simeone, G.J. Thorogood, D. Huo, L. Luneville, G. Baldinozzi, V. Petricek, F. Porcher, J. Ribis, L. Mazerolles, L. Largeau, J.F. Berar, S. Surble, Intricate disorder in defect fluorite/pyrochlore: a concord of chemistry and crystallography, Sci. Rep. 7 (2017) 3727.
[11] B.P. Mandal, P.S.R. Krishna, A.K. Tyagi, Order–disorder transition in the $Nd_{2-y}Y_yZr_2O_7$ system: Probed by X-ray diffraction and Raman spectroscopy, J. Solid State Chem. 183 (2010) 41–45.
[12] B.P. Uberuaga, M. Tang, C. Jiang, J.A. Valdez, R. Smith, Y. Wang, K.E. Sickafus, Opposite correlations between cation disordering and amorphization resistance in spinels versus pyrochlores, Nat. Commun. 6 (2015) 8750.
[13] K.E. Sickafus, R.W. Grimes, J.A. Valdez, A. Cleave, M. Tang, M. Ishimaru, S. M. Corish, C.R. Stanek, B.P. Uberuaga, Radiation-induced amorphization resistance and radiation tolerance in structurally related oxides, Nat. Mater. 6 (2007) 217–223.
[14] J. Wang, F. Zhang, J. Lian, R.C. Ewing, U. Becker, Energetics and concentration of defects in $Gd_2Ti_2O_7$ and $Gd_2Zr_2O_7$ pyrochlore at high pressure, Acta Mater. 59 (2011) 1607–1618.
[15] K. Sickafus, L. Minervini, R. Grimes, J. Valdez, M. Ishimaru, F. Li, K. McClellan, T. Hartmann, Radiation tolerance of complex oxides, Science 289 (2000) 748–751.
[16] J. Shamblin, M. Feygenson, J. Neuefeind, C.L. Tracy, F. Zhang, S. Finkeldei, D. Bosbach, H. Zhou, R.C. Ewing, M. Lang, Probing disorder in isometric pyrochlore and related complex oxides, Nat. Mater. 15 (2016) 507–511.
[17] F. Zhao, S. Hu, C. Xu, H. Xiao, X. Zhou, X. Zu, S. Peng, Probing local site disorder in zirconate pyrochlores, Ceram. Int. 49 (2023) 18432–18441.
[18] E.C. O'Quinn, K.E. Sickafus, R.C. Ewing, G. Baldinozzi, J.C. Neuefeind, M. G. Tucker, A.F. Fuentes, D. Drey, M.K. Lang, Predicting short-range order and correlated phenomena in disordered crystalline materials, Sci. Adv. 6 (2020) eabc2758.
[19] B.P. Uberuaga, Intricate disorder, Nat. Mater. 15 (2016) 496–497.
[20] U. Matsumoto, T. Ogawa, S. Kitaoka, H. Moriwake, I. Tanaka, First-Principles Study on the Stability of Weberite-Type, Pyrochlore, and Defect-Fluorite Structures of $A_2^{3+}B_2^{4+}O_7$ (A = Lu3+–La3+, B = Zr4+, Hf4+, Sn4+, and Ti4+), J. Phys. Chem. C 124 (2020) 20555–20562.
[21] P.M. Kowalski, Formation enthalpy of $Ln_2B_2O_7$-type (B= Ti, Sn, Hf, Zr) compounds, Scr. Mater. 189 (2020) 7–10.
[22] K.M. Turner, D.R. Rittman, R.A. Heymach, C.L. Tracy, M.L. Turner, A.F. Fuentes, W.L. Mao, R.C. Ewing, Pressure-induced structural modifications of rare-earth hafnate pyrochlore, J. Phys. Condens. Matter 29 (2017) 255401.
[23] G. Kresse, J. Furthmüller, Efficiency of ab-initio total energy calculations for metals and semiconductors using a plane-wave basis set, Comput. Mater. Sci 6 (1996) 15–50.
[24] G. Kresse, J. Furthmüller, Efficient iterative schemes for ab initio total-energy calculations using a plane-wave basis set, Phys. Rev. B 54 (1996) 11169.
[25] P.E. Blöchl, Projector augmented-wave method, Phys. Rev. B 50 (1994) 17953.
[26] J.P. Perdew, K. Burke, M. Ernzerhof, Generalized gradient approximation made simple, Phys. Rev. Lett. 77 (1996) 3865.
[27] A. van de Walle, P. Tiwary, M. de Jong, D.L. Olmsted, M. Asta, A. Dick, D. Shin, Y. Wang, L.Q. Chen, Z.K. Liu, Efficient stochastic generation of special quasirandom structures, Calphad 42 (2013) 13–18.
[28] U. Matsumoto, Crystal Structure and Oxide Ion Diffusion in Pyrochlore Related Oxides, (2022).
[29] C.G. Liu, Y.H. Li, Y.D. Li, L.Y. Dong, J. Wen, D.Y. Yang, Q.L. Wei, P. Yang, First principle calculation of helium in $La_2Zr_2O_7$: Effects on structural, electronic properties and radiation tolerance, J. Nucl. Mater. 500 (2018) 72–80.
[30] C. Liu, Q. Peng, T. Shi, F. Gao, Y. Li, Physical properties and radiation tolerance of high-entropy pyrochlores $Gd_2(Ti_{0.25}Zr_{0.25}Sn_{0.25}Hf_{0.25})_2O_7$ and individual pyrochlores $Gd_2X_2O_7$ (X= Ti, Zr, Sn, Hf) from first principles calculations, Scr. Mater. 220 (2022) 114898.
[31] M. Li, P. Li, H. Xiao, H. Zhang, X. Zu, A DFT+U study on the thermodynamic properties of defective $Gd_2Zr_2O_7$ pyrochlore, J. Nucl. Mater. 542 (2020) 152425.
[32] S.F. Pugh, Xcii., Relations between the elastic moduli and the plastic properties of polycrystalline pure metals, The London, Edinburgh, and Dublin Philosophical Magazine and Journal of Science 45 (1954) 823–843.
[33] F.A. Zhao, H.Y. Xiao, X.M. Bai, Z.J. Liu, X.T. Zu, Effects of doping Yb^{3+}, La^{3+}, Ti^{4+}, Hf^{4+}, Ce^{4+} cations on the mechanical properties, thermal conductivity, and electronic structures of $Gd_2Zr_2O_7$, J. Alloy. Compd. 776 (2019) 306–318.